

# From Microparticles to Nanowires and Back: Radical Transformations in Plated Li Metal Morphology Revealed via *in Situ* Scanning Electron Microscopy

Alexander Yulaev,<sup>\*,†,‡,§</sup> Vladimir Oleshko,<sup>||</sup> Paul Haney,<sup>†</sup> Jialin Liu,<sup>⊥</sup> Yue Qi,<sup>⊥</sup> A. Alec Talin,<sup>#</sup> Marina S. Leite,<sup>‡,∇</sup> and Andrei Kolmakov<sup>\*,†,||</sup>

<sup>†</sup>Center for Nanoscale Science and Technology, National Institute of Standards and Technology (NIST), Gaithersburg, Maryland 20899, United States

<sup>‡</sup>Department of Materials Science and Engineering, University of Maryland, College Park, Maryland 20742, United States

<sup>§</sup>Maryland NanoCenter, University of Maryland, College Park, Maryland 20742, United States

<sup>||</sup>Materials Science and Engineering Division, National Institute of Standards and Technology (NIST), Gaithersburg, Maryland 20899, United States

<sup>⊥</sup>Department of Chemical Engineering and Materials Science, Michigan State University, East Lansing, Michigan 48824, United States

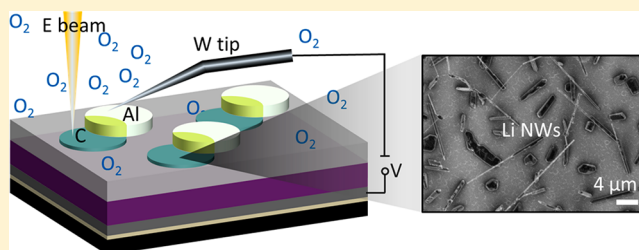
<sup>#</sup>Sandia National Laboratories, Livermore, California 94551, United States

<sup>∇</sup>Institute for Research in Electronics and Applied Physics, University of Maryland, College Park, Maryland 20742, United States

## Supporting Information

**ABSTRACT:** Li metal is the preferred anode material for all-solid-state Li batteries. However, a stable plating and stripping of Li metal at the anode–solid electrolyte interface remains a significant challenge particularly at practically feasible current densities. This problem usually relates to high and/or inhomogeneous Li–electrode–electrolyte interfacial impedance and formation and growth of high-aspect-ratio dendritic Li deposits at the electrode–electrolyte interface, which eventually shunt the battery. To better understand details of Li metal plating, we use *operando* electron microscopy and Auger spectroscopy to probe nucleation, growth, and stripping of Li metal during cycling of a model solid-state Li battery as a function of current density and oxygen pressure. We find a linear correlation between the nucleation density of Li clusters and the charging rate in an ultrahigh vacuum, which agrees with a classical nucleation and growth model. Moreover, the trace amount of oxidizing gas ( $\approx 10^{-6}$  Pa of  $O_2$ ) promotes the Li growth in a form of nanowires due to a fine balance between the ion current density and a growth rate of a thin lithium-oxide shell on the surface of the metallic Li. Interestingly, increasing the partial pressure of  $O_2$  to  $10^{-5}$  Pa resumes Li plating in a form of 3D particles. Our results demonstrate the importance of trace amounts of preexisting or ambient oxidizing species on lithiation processes in solid-state batteries.

**KEYWORDS:** *In situ*, scanning electron microscopy, all-solid-state batteries, carbon anode, lithium plating



Li metal is an attractive anode material for all-solid-state Li batteries (SSLBs) due to its high theoretical capacity (3860 mA h/g) and low potential vs standard hydrogen electrode ( $-3.04$  V).<sup>1–3</sup> To match the energy capacity of a typical Li-ion cell, a relatively thick Li metal film of  $\approx 20$   $\mu\text{m}$  is needed.<sup>4</sup> However, achieving a stable plating and stripping of Li metal in contact with a solid-state electrolyte (SSE) yet remains a significant technological challenge, even when the Li–SSE interface is thermodynamically or kinetically stabilized.<sup>4,5</sup> The current experimental effort is dedicated to achieving homogeneous plating/stripping of such a thick layer, avoiding destructive mechanical strains in the anode, and minimizing the impedance of electrode–SSE interfaces.<sup>6–10</sup> An additional problem with Li anodes is the observed shorting of the cells by

metallic Li filaments growing through grain boundaries of crystalline SSEs.<sup>11</sup> The aforementioned SSLB challenges become particularly critical for current densities exceeding  $\approx 1$  mA/cm<sup>2</sup>, which is still below the  $>10$  mA/cm<sup>2</sup> requirement for portable electronics and electric vehicle applications.<sup>12</sup>

Recently, *in situ* transmission electron microscopy revealed the selective role of oxygen, nitrogen gases, and water vapor on passivation and corrosion of Li metal surface during battery operation.<sup>13</sup> Similarly, *operando* optical<sup>14</sup> and SEM<sup>15</sup> character-

**Received:** October 23, 2017

**Revised:** January 9, 2018

**Published:** February 3, 2018

ization of Li plating in electrochemical cells highlighted the role of the solid electrolyte interphase (SEI) on Li dendrite growth. Further advances in controlling Li morphology, however, require detailed understanding of Li growth mechanism during plating and dissolution, as well as the effects that the substrate and the surrounding environment (i.e., adsorbates) have on this process.<sup>15–19</sup>

Previously, we used *operando* ultrahigh vacuum-SEM (UHV-SEM) to monitor in real time the microstructure evolution of an Al anode during its lithiation and delithiation reactions and demonstrated how chemical side reactions on the anode surface and anode–current collector interface can affect the battery capacity retention.<sup>20,21</sup> Here, we extend this approach to characterize Li metal plating and stripping at a model ultrathin carbon anode deposited on an amorphous, nitrogen doped lithium phosphate (LiPON) SSE/LiCoO<sub>2</sub> cathode stack. Our observations reveal a linear correlation between the nucleation density of Li clusters and the charging rate under UHV conditions, which agrees well with the classical 2D model of nucleation and growth. We find that the morphology of metallic Li deposition is highly sensitive to the oxidizing ambient and drastically changes from mostly in-plane 3D particle growth mode under UHV conditions to out-of-plane whisker-like growth once the oxygen pressure in UHV chamber increases from  $\approx 10^{-7}$  to  $\approx 10^{-6}$  Pa. The in-plane Li growth mode reestablishes once the oxygen pressure further rises to  $10^{-5}$  Pa. We attribute the change in the Li growth mode to the formation of an encapsulating lithium-oxide surface layer that controls the morphology of a growing Li nanoparticle.

A schematic of the thin film battery and the experimental setup are illustrated in Figure 1. Arrays of SSLBs are fabricated

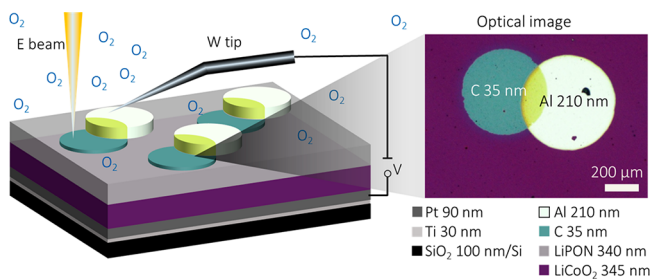


**Figure 1.** (Left) A schematic of the experimental setup used to cycle the all-solid-state batteries in an *operando* SEM with the controlled pressure of O<sub>2</sub>. The grounded tungsten (W) tip is used to contact the C–Al anode. A potential is applied to the Pt–Ti current collector electrode to charge/discharge the electrochemical cell. (Right) Real-color optical image of C–Al anode in a representative device.

on a Si (001) wafer covered with a 100 nm thermal SiO<sub>2</sub>. A 90 nm Pt/30 nm Ti current collector is deposited using an electron beam evaporation followed by a  $\approx 345$  nm thick LiCoO<sub>2</sub> cathode sputtered using previously described conditions.<sup>22</sup> Following deposition, the LiCoO<sub>2</sub> is annealed in the O<sub>2</sub> atmosphere at 700 °C for 2 h to form the high-temperature phase. A  $\approx 340$  nm thick LiPON electrolyte layer is sputtered on top of the cathode layer. Next, an array of amorphous carbon (C) anodes with a thickness of  $\approx 35$  nm is evaporated through a stencil mask with a diameter of 0.51 mm. Then,  $\approx 210$  nm thick Al pads have been evaporated through the same shadow mask but with an offset to leave most of the C-anode surface exposed. The Al pads are used to make electrical contact with the C anodes.

All *operando* measurements are carried out in a UHV-SEM setup with a residual gas pressure of  $\approx 10^{-7}$  Pa which is equipped with microprobes, scanning Auger electron spectroscopy (AES), X-ray photoelectron spectroscopy (XPS), and gas inlet system.<sup>21</sup> Electrochemical charging and discharging of the SSLBs are conducted using a commercial current voltage source-measure unit in a 2-electrode configuration with the cathode serving as the working electrode and the anode as the counter and reference electrode. Characterization of pristine C anodes using Raman spectroscopy and high-resolution analytical transmission electron microscopy shows that the thin C films are amorphous, without pores, and composed of nm size clusters (Figure S1a,c). Electron energy-loss spectroscopy (EELS) (Figure S1e,f) and XPS (Figure S1d) reveal the predominantly sp<sup>3</sup> nature of carbon bonds in the anode films. XPS also indicates an appreciable presence of the C–O, carbonyl, carboxyl, and hydroxyl groups at the surface of carbon anode, formed presumably during the sample transfer and exposure to ambient air. Conversely, local energy dispersive X-ray spectroscopy (EDXS) of the carbon films shows rather low oxygen bulk concentration (Figure S1b). To study the effect of reactive ambient on Li plating, the controlled leak of the pure oxygen was admitted to the UHV chamber. The real-time mass spectrometry of the residual and admitted gases was used to monitor the composition of the chamber ambient (Figure S2).

We begin with the nucleation and growth of Li on the C anode during low current density galvanostatic battery charging under UHV conditions ( $P < 6 \times 10^{-7}$  Pa, Figure 2). The initial stage of C-anode lithiation can be experimentally observed as a gradual and spatially homogeneous SEM brightness (secondary electron yield) change of the entire carbon pad upon battery biasing (similar to the brightness evolution seen in the top two rows in Figure S3). During this stage Li freely lithiates amorphous carbon, passing through all the intermediate phases in the Li–C phase diagram<sup>23</sup> until it reaches the intercalation limit. No Li particles are observed at this stage yet. Segregation of metallic Li nuclei visible in Figure 2a starts with oversaturation of the C anode with Li. The characteristic particle faceting observed in Figure 2a is consistent with the formation of crystalline body-centered cubic (BCC) metallic Li islands. During slow charging ( $< 0.3$  mA/cm<sup>2</sup>), neither frontal nor cross-sectional SEM reveal any visible cracks in the anode layer due to Li deposition at the LiPON–carbon interface. This is due to two reasons: (i) high Li diffusion in amorphous C ( $\approx 10^{-10}$  cm<sup>2</sup>/s) exceeding by approximately 1 order of magnitude the diffusion coefficient in LiPON; (ii) the absence of any volumetric confinement for Li at the free vacuum–carbon interface. Thus, Li cluster nucleation barrier on the C-anode surface is smaller compared to one at the carbon–electrolyte interface.

Figure 2b shows the areal density of Li clusters measured as a function of the state-of-charge at current densities of 0.026, 0.08, 0.17, and 0.26 mA/cm<sup>2</sup> (for SEM images, see Figure S4). Independently of the charging rate, Li nucleation initiates at  $\approx 2.5 \times 10^{-4}$  C of injected charge and  $\approx 4$  V, which is seen as a “kink” in the potential versus the state-of-charge curve (Figure 2c). The number of Li nuclei grows rapidly until it reaches a steady state when no new particles appear, indicating that Li transported from the cathode to the anode contributes predominantly to the growth rather than to nucleation of new particles. In order to quantify the Li nucleation kinetics under UHV conditions, we adopt a classical thin film nucleation and growth model (see reviews<sup>24,25</sup> and references therein).

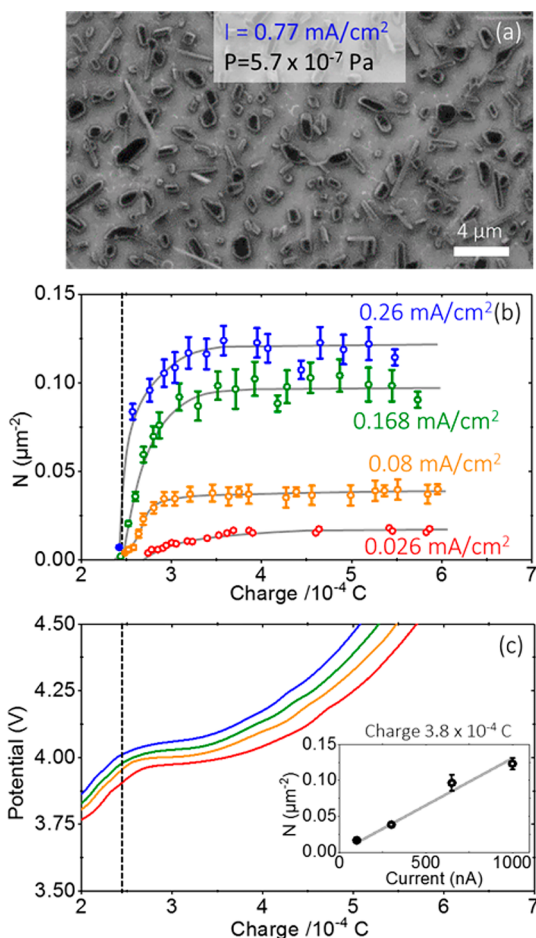


**Figure 2.** Dependence of the Li particle nucleation density on the charging rate. (a) SEM image depicting Li plating at the carbon anode of the battery charged under UHV conditions. (b) Nucleation density estimated from the SEM images (Figure S4) and (c) potential as a function of the battery state-of-charge for 0.026 mA/cm<sup>2</sup> (red), 0.08 mA/cm<sup>2</sup> (orange), 0.168 mA/cm<sup>2</sup> (green), and 0.26 mA/cm<sup>2</sup> (blue), respectively. The error bars correspond to the uncertainty of particle recognition at the borders of the SEM field of view. Gray lines in part b serve as a guide to the eye. The inset in part c depicts the nucleation density behavior,  $N$ , versus the charging current at a steady state.

According to this approach, guest atoms deposited onto the host substrate form either continuous films or discontinuous nanostructures depending on the thermodynamic and kinetic parameters. By analogy with this model, Li<sup>+</sup> ions are driven from the cathode through the SSE to the C anode during battery charging and become reduced to metallic state at the anode. Upon oversaturation of the C anode, Li atoms nucleate to form Li clusters on the anode-free surface, and then grow as Li microparticles. The average secondary electron (SE) yield of metallic lithium is lower compared to amorphous C,<sup>26,27</sup> resulting in corresponding contrast differences in SEM images (Figure 2a). Following the close analogy between electrochemical Li plating and film growth by physical vapor deposition, the nucleation density of Li particles,  $N$ , in a steady state in a vacuum can be expressed in terms of scaling relation:<sup>24</sup>

$$N \propto \left(\frac{J}{D}\right)^{z/z+2} \quad (1)$$

Here,  $J$ ,  $D$ , and  $z$  stand for the current (flux of Li atoms), surface diffusion coefficient, and a minimal number of atoms in a thermodynamically stable cluster. Usually, the critical nucleus consists of a few hundred atoms,<sup>28</sup> and therefore, the nucleation density should be linearly proportional to the current at a constant diffusion coefficient. We observe this dependence in our experimental data (see inset in Figure 2c) validating the applicability of this approach to our system. The obtained results corroborate qualitatively with the previous *ex situ* SEM results on Li deposition from a liquid electrolyte.<sup>29</sup>

The aforementioned Li growth mechanism alters once the charging rate increases in excess of  $\approx 1$  mA/cm<sup>2</sup>, at which point Li deposition can also occur at the C–LiPON interface. Under high current densities, the ionic flux balance conditions at the anode–electrolyte interface are not fulfilled anymore, leading to Li accumulation in the anode, mechanical stress development, film cracking, and micron thick whiskers growth from their roots (Figure S5 and the SI video). Interestingly, the footprints of these Li whiskers are located at the periphery of the topographic features resembling the grain boundaries. The size of these features approximately correlates with underlying LiCoO<sub>2</sub> grain size convoluted with a conformal coverage of amorphous LiPON layer. As it has been shown in previous reports, Li-ion flux across LiPON/LiCoO<sub>2</sub> solid-state batteries is not spatially homogeneous at the nanoscale, and Li ions evolve predominantly from the electrochemically active LiCoO<sub>2</sub> {010} grain facets.<sup>30</sup> At charging rates exceeding 1 mA/cm<sup>2</sup>, Li lateral diffusion is not fast enough to match the incoming flux of the Li ions, and therefore the grain structure of the buried LiCoO<sub>2</sub> layer becomes “projected” to a C-anode surface determining the location of the nucleation and growth sites of Li whiskers and microparticles. However, at lower charging rates (Figure S4), the lateral diffusion of Li in C anode is fast enough to smooth the nanoscopic inhomogeneities of Li source. This is supported by observing Li nucleation at random locations on a C anode, which are not necessary correlated with grain boundary sites (Figure S4).

We now consider the effect of reactive gaseous environment on morphology of Li deposits. Due to high reactivity, the nucleation and growth of Li on the carbon-anode surface during battery charging can be affected by (i) the preabsorbed/dissolved oxygen containing species and (ii) those adsorbed from the ambient during cycling. XPS data (Figure S6) collected *in situ* from the pristine anode under UHV conditions indicate that the as-prepared carbon surface already contains a noticeable amount of oxygen species. Those species, however, become consumed either via reaction with Li diffused from LiPON and/or during the first battery cycle and do not affect the long-term battery performance or Li plating morphology recorded under UHV. This is confirmed by an only minor change in intensity of O 1s peak during SSLB cycling while Li 1s intensity and corresponding C 1s attenuation due to Li drastically increase under the same conditions.

To elucidate the role of oxidizing species from ambient environment, we study Li plating as a function of O<sub>2</sub> partial pressure in the range from  $\approx 5 \times 10^{-7}$  to  $\approx 5 \times 10^{-5}$  Pa. The comparative local AES analysis of the particle-free C-anode areas and plated Li particles surfaces indicate that (i) both partitions become irreversibly oxidized with time during SSLB cycling at  $5 \times 10^{-7}$  Pa, and (ii) the degree of oxidation of lithiated carbon layer is larger compared to grown Li nanoparticles (Figures S7 and S8). SEM images in Figure 3a–c depict the galvanotactic Li plating at 0.77 mA/cm<sup>2</sup>

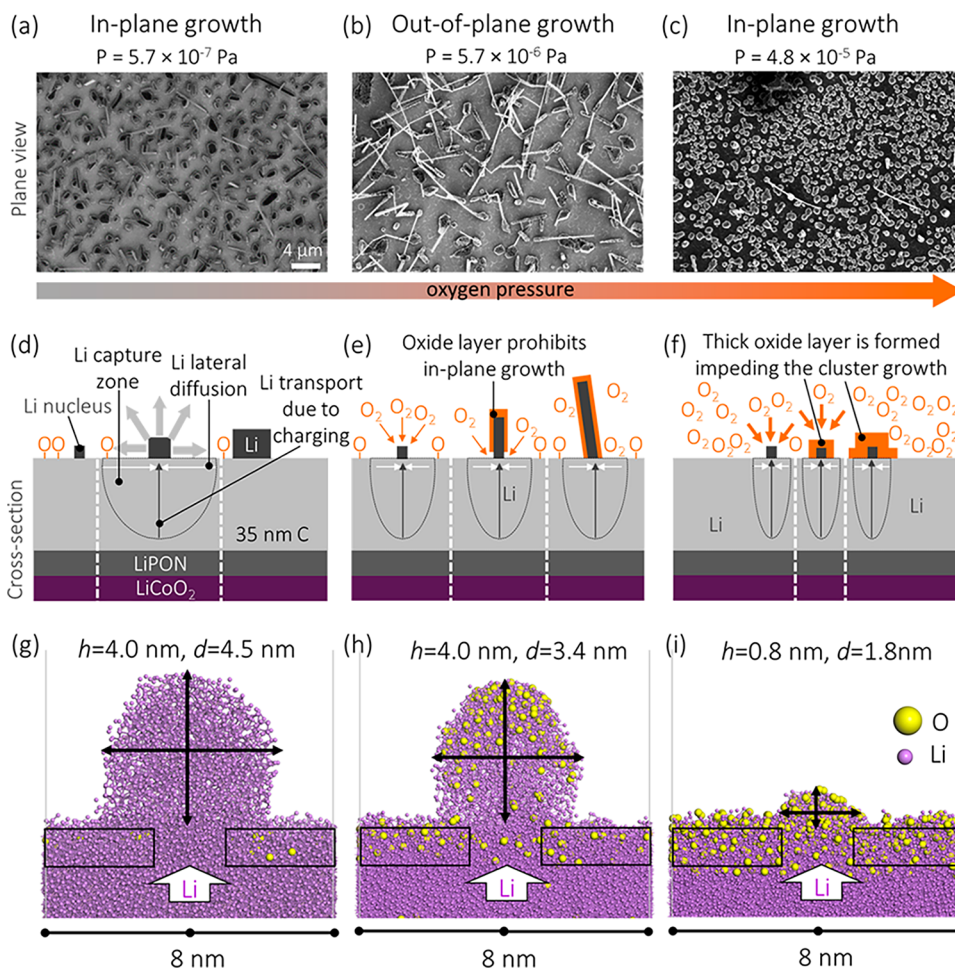


**Figure 3.** Effect of oxygen pressure on Li plating morphology. (a–c) SEM images of Li plated at  $5.7 \times 10^{-7}$ ,  $5.7 \times 10^{-6}$ , and  $4.8 \times 10^{-5}$  Pa residual oxygen pressure, respectively;  $0.77 \text{ mA/cm}^2$  current density. (d–f) Schematics showing models of the Li nucleation and growth for the images presented in parts a–c. In the presence of  $\text{O}_2$ , a lithium-oxide sheath is developed. Schematics are drawn not to scale. The SEM images are acquired at  $\approx 0.04 \text{ mA h/cm}^2$  capacity of deposition. (g–i) MD simulation snapshots of Li grown under (g) UHV, (h) oxygen atmosphere, and (i) oxygen atmosphere at increased temperature to reach a higher oxidation rate after 50 ps for parts g and i and 55 ps for part h, respectively.

current density (see voltage profiles in Figure S9) under  $5.7 \times 10^{-7}$ ,  $5.7 \times 10^{-6}$ , and  $4.8 \times 10^{-5}$  Pa oxygen pressure, respectively. Interestingly, Li deposit morphology changes from the mainly in-plane 3D growth of metallic Li islands with a negligible fraction of nanowires, to one dominated by nanowire growth as the  $\text{O}_2$  pressure increases by 1 order of magnitude from  $\approx 6 \times 10^{-7}$  to  $\approx 6 \times 10^{-6}$  Pa. In-plane Li 3D particles growth mode is again reestablished as the  $\text{O}_2$  partial pressure is further increases to  $\approx 5 \times 10^{-5}$  Pa. Moreover, the nucleation density of Li particles triples once the oxygen pressure grows from  $\approx 6 \times 10^{-7}$  to  $\approx 5 \times 10^{-5}$  Pa (Figure 3a–c, and Figure S10).

The proposed mechanism for the effect of surface oxidation on the Li deposit morphology is depicted in Figure 3d–f. We state that the interplay between the Li current densities and surface oxidation rate of growing Li nanostructures is responsible for drastic changes in morphology of Li deposits. The morphology of deposits evolves as 3D particles under UHV (Figure 3a,d) and highly oxidizing ambient (Figure 3c,f) and changes to quasi-1D submicron thin nanowires when plating takes place at  $\approx 6 \times 10^{-6}$  Pa of oxygen partial pressure (Figures 3b,e). The formation of Li-core/oxide-shell structure around growing Li deposits is known from previous studies,<sup>31</sup> and also supported by our AES measurements (Figures S7 and

S8) and SEM imaging of contrast reversal between C anode and Li-oxide deposits due to higher secondary electron yield. The development of Li-oxide shells around the growing metallic nanowires is further evidenced via SEM imaging of the same anode region before and after Li discharge (Figure 4a,b). The images show bright, solid shells with thickness of few tens of nanometers remaining after the metallic Li core is intercalated back into  $\text{LiCoO}_2$  during battery discharge.

For an intermediate oxygen pressure range  $\approx 6 \times 10^{-6}$  Pa, the O atomic flux rate is  $\approx 5 \times 10^{13} (\text{s cm}^2)^{-1}$ , which is 100 times smaller than the Li current density  $J$ . The growing Li surface becomes gradually oxidized. The thickness,  $h$ , of the newly formed oxide depends of the Li-ion diffusion,  $D$ , in the oxide (Li ions/vacancies diffuse significantly faster than oxygen does), oxygen partial pressure,  $P$ , and exposure time,  $t$ , and can be described as<sup>32</sup>

$$h = \sqrt{\frac{2DKP}{N_1} t} \quad (2)$$

Here,  $N_1$  is the number of oxygen atoms in Li-oxide unit cell, and  $K$  is the Henry's law constant. The presence of a thin oxide sheath prevents the surface from the rapid bulk oxidation and inhibits Li surface diffusion<sup>33,34</sup> due to the high activation

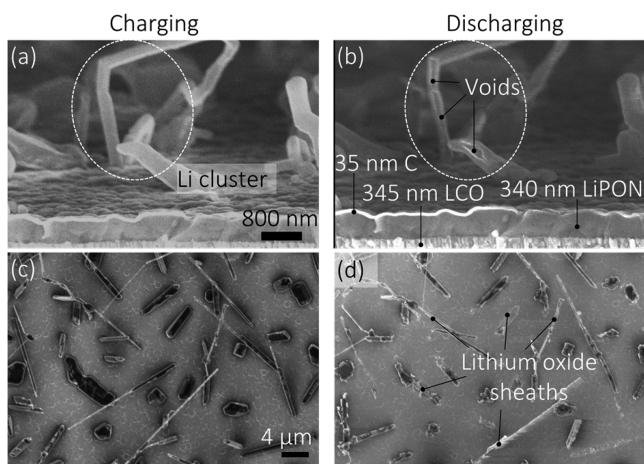


**Figure 4.** (a, b) Cross-section and (c, d) top-view secondary electron images showing Li wires during battery charging and discharging. Upon discharging, voids are formed in the middle of wires due to dissolution of metallic Li, leaving behind only Li-oxide sheaths at the carbon anode.

energy. Therefore, volume expansion during charging can only occur through the footprint of the Li particles via the out-of-plane elongation (Figure 3e). As Li nanowires grow, a newly emerged Li surface at the wire footprint gets oxidized and encapsulated, thus promoting a one-dimensional growth (Figure 3e) from a catalytic center akin to the vapor–liquid–solid growth mechanism of metal-oxide nanowires or the oxygen assisted growth of Si nanowires.<sup>35</sup> Similarly, a thin oxide layer is formed also at the surface of Li saturated carbon anode. Since more Li accumulates inside the C anode, a developing compressive stress is channeling Li to existing growth spots. Finally, an additional driving force for 1D growth develops due to the progressive Li nanowire surface oxidation. Due to higher density of  $\text{Li}_x\text{O}$  compared to metallic Li, the surface oxide layer induces a compressive stress on a NW metallic core. The stress can release via directed flow of the metallic Li toward the NW footprint.

This 1D Li growth proceeds until partial oxygen pressure reaches the level where a sufficiently thick oxide layer is formed around the Li nuclei and at the surface of the lithiated carbon. At this pressure, the thickness of the oxide near the Li particle footprint reaches the critical magnitude  $h_{\max} \geq \frac{\tau_Y L_z}{\sigma_f}$ , where it will not fracture upon the given compressive stress in the C anode. Here,  $\tau_Y$  is the shear stress at the Li– $\text{Li}_2\text{O}$  interface,  $\sigma_f$  is the oxide fracture strength,  $L_z$  is the distance between the Li NW tip and the stress-free end of the oxide layer.<sup>36</sup> Note, this mechanically robust oxide shell is formed around each cluster including regions close to the root of the Li nanostructures (Figure 3f), pinning Li deposits to the C-anode surface and inhibiting any further growth. Since the potential barrier for particle nucleation is proportional to  $\gamma^3$ , where  $\gamma$  is the surface energy of Li, oxidation of Li leads to surface energy increase of the Li–O interface, resulting in potential barrier growth.<sup>28</sup> Therefore, the Li flux,  $J$ , contributes mostly to nucleation of new Li nanostructures which are more energetically favorable rather than to the growth of the pre-existing ones, in a manner analogous to metal electroplating from solution in the presence of brightening agent such as saccharin.<sup>37</sup>

The observed changes in the nucleation density at elevated oxygen partial pressure can be also qualitatively explained using

the aforementioned 2D Li nucleation and growth model. For that, we have extended the model by introducing the second species ( $\text{O}_2$ ) diffusing across the C anode. Following the atomistic nucleation formalism for oxygen and lithium atoms, we modify eq 1 using the generalized formula for two species:

$$N \propto \left( (z + k + 2)(\sigma_{\text{Li}}J + \sigma_{\text{O}}P) \frac{I^z P^k}{D} \right)^{1/(z+k+2)} \quad (3)$$

Here,  $P$ ,  $\sigma_{\text{Li}}$ ,  $\sigma_{\text{O}}$ ,  $z$ , and  $k$  represent the oxygen pressure, dimensionless capture numbers accounting for the propensity of clusters to absorb Li or O adatoms, and a minimal number of Li and O atoms in a stable cluster, respectively. For negligible amount of oxygen,  $P \approx 0$  and  $k \approx 0$ , the expression 2 reduces to eq 1. In case of significant oxygen flux, a critical cluster is reduced to only a few atoms, and dependence of  $N$  on Li current and oxygen pressure becomes sublinear semiquantitatively supporting the experimental results for in-plane growth modes observed under  $10^{-5}$  Pa oxygen gas pressure conditions (Figure S10). The proposed 2D theory agrees with the observed nucleation density of Li deposits at  $10^{-7}$  and  $10^{-5}$  Pa where the Li morphology does not play a significant role during nucleation. To understand the effect of nanowire morphology on a nucleation density at  $10^{-6}$  Pa, one can consider Li nanowires as a “Li sink” that eliminates some part of Li atoms from a lateral diffusion and nucleation processes. In this case, the nucleation density would decrease since the amount of Li responsible for particle nucleation would be reduced by a difference between the current inflow due to charging and the outflow to Li sinks.

To capture the dynamics of lithium growth and oxidation at an early stage, a molecular dynamics (MD) simulation with the ReaxFF force field<sup>38</sup> is performed. As shown in Figure 3g–i, the Li atoms in an  $8 \text{ nm} \times 8 \text{ nm} \times 10 \text{ nm}$  Li slab are extruded from a 2 nm diameter circle on the surface, as the rest of the surface atoms (within the boxed area) are fixed. Due to the size and time scale limitations inherent to MD simulations, only the initial growth of Li in the three environments is investigated. During the initial formation stage, the oxide layer thickness evolution can be approximated with a linear growth relationship,<sup>32</sup> as  $h = CPt$ , where  $C$  is related to the temperature dependent reaction rates and Henry’s law constant  $K$ . In MD simulations, both the oxygen pressure,  $P$ , and temperature can be tuned to control the oxidation rate to compete with the Li growth rate.

Figure 3g–i clearly shows that, with the increased oxidation rate and oxide layer thickness, less Li grows out of the surface, as the oxide layer imposes a compressive stress to resist free Li growth. This is consistent with the experimental observation that the nucleation at higher  $\text{O}_2$  pressure proceeds with a minor increase in overpotential to break very thin oxide sheath formed on top of the anode. As shown in Figure 3g, metallic Li uniformly grows in all 3D directions resulting in a sphere shape under UHV. With much faster oxidation rate (Figure 3i), not only is the Li particle completely oxidized, but it also wets the oxide surface and expands mainly along the in-plane directions. Figure 3h demonstrates a  $\approx 5$  times faster Li growth rate than the oxygen atom incorporation rate (thus a thin surface oxide layer forms). We observe that as Li metal gets partially oxidized, it displays a higher aspect ratio than that in Figure 3g and 3i. The surface oxide layer shrinks in volume due to the higher density of  $\text{Li}_x\text{O}$  than metallic Li. Since  $\text{Li}_x\text{O}$  is not an effective passivation layer compared to, e.g.,  $\text{Al}_2\text{O}_3$ ,<sup>39</sup> the oxide cracks

and exposes a pristine Li surface to oxidizing species. Therefore, experimentally, we observe that Li particles of a few tens of nanometers in diameter can be completely oxidized during the 10–20 min long experiments.

Grazing angle SEM imaging of Li plating (Figure S5) supports the root growth mechanism of the out-of-plane Li deposits. Using the kink in the Li nanowire as a fiducial point, one can notice that the growth occurs at the Li nanostructure–carbon interface, pushing the whole wire in the direction normal to the C-anode plane.

Finally, we have noticed an interesting “catalytic” effect of the electron beam irradiation that locally increases the oxidation rate of Li due to the electron beam induced oxygen dissociation.<sup>40</sup> The latter can suppress wire growth even at a lower background pressure of O<sub>2</sub> (Figure S11a). This observed effect can be used for local controlling Li oxidation with a nano- and microscale resolution.

In summary, UHV *operando* SEM studies using a model thin film solid-state battery system provide new insights into the mechanisms of early stage Li plating and the surprising effects of oxidant on the Li nanostructure growth. In particular, we showed that, under UHV or relatively high oxygen partial pressure (in excess of  $\approx 10^{-5}$  Pa), a low-rate ( $\leq 1$  mA/cm<sup>2</sup>) Li plating proceeds via nucleation and growth of 3D particles. However, at intermediate O<sub>2</sub> partial pressure of  $\approx 10^{-6}$  Pa, the oxide sheath forming around the growing Li nanostructures promotes the Li deposit evolution in the form of 1D nanowires. This transition is largely controlled by the thickness of the oxide layer formed on the Li surface and therefore strongly depends on the charging rate ( $J$ ) and oxide thickness growth ( $\frac{dh}{dt}$ ) rates. We anticipate that the conditions favoring 1D growth can exist in a wide range of  $J\left(\frac{dh}{dt}\right)^{-1}$  ratios (see Table S1 and related discussion there). Rapid charging, however, leads to Li segregation inside the volume of the anode, compressive stress development, cracking/delamination followed by Li metal creeping at the interfaces, and large whisker growth independent of ambient conditions.

## ■ ASSOCIATED CONTENT

### ● Supporting Information

The Supporting Information is available free of charge on the ACS Publications website at DOI: 10.1021/acs.nanolett.7b04518.

Amorphous carbon characterization, mass spectrometry of the residual gas, *operando* SEM and AES probing C lithiation and Li plating, *operando* XPS characterization of Li deposition onto the carbon anode, voltage profiles of Li deposition, SEM of electron beam induced effect, MD simulations of Li nucleation and growth, and table showing the expected Li growth morphology at different charging rate and oxygen pressure (PDF)  
Li particle growth (AVI)

## ■ AUTHOR INFORMATION

### Corresponding Authors

\*E-mail: alexander.yulaev@nist.gov.

\*E-mail: andrei.kolmakov@nist.gov.

### ORCID

Alexander Yulaev: 0000-0002-9225-3448

Vladimir Oleshko: 0000-0003-0538-2354

Yue Qi: 0000-0001-5331-1193

A. Alec Talin: 0000-0002-1102-680X

Marina S. Leite: 0000-0003-4888-8195

Andrei Kolmakov: 0000-0001-5299-4121

### Author Contributions

All authors contributed to and approved the manuscript.

### Notes

The authors declare no competing financial interest.

## ■ ACKNOWLEDGMENTS

A.Y. and M.S.L. acknowledge support under the Cooperative Research Agreement between the University of Maryland and the National Institute of Standards and Technology Center for Nanoscale Science and Technology, Award 70NANB14H209, through the University of Maryland. M.S.L. thanks the Center for Research in Extreme Batteries (CREB). J.L. and Y.Q. acknowledge the support from the Department of Energy, Office of Energy Efficiency and Renewable Energy (EERE), under the Award DE-EE0007803. A.A.T. was supported by Nanostructures for Electrical Energy Storage (NEES), an Energy Frontier Research Center (EFRC) funded by the U.S. Department of Energy, Office of Science, Office of Basic Energy Sciences under Award DESC0001160 and by Sandia’s Laboratory-Directed Research and Development program. Sandia National Laboratories is a multitechnology laboratory managed and operated by National Technology and Engineering Solutions of Sandia, LLC., a wholly owned subsidiary of Honeywell International, Inc., for the U.S. Department of Energy’s National Nuclear Security Administration under Contract DE-NA-0003525. The authors are thankful to Dr. N. Zhitenev (NIST), Dr. Dmitry Ruzmetov (ARL/NIST), and Prof. J. Cumings (UMD) for constructive feedback on the manuscript.

## ■ REFERENCES

- (1) Tarascon, J.-M.; Armand, M. *Nature* **2001**, *414*, 359–367.
- (2) Armand, M.; Tarascon, J.-M. *Nature* **2008**, *451*, 652–657.
- (3) Chu, S.; Majumdar, A. *Nature* **2012**, *488*, 294–303.
- (4) Janek, J.; Zeier, W. G. *Nat. Energy* **2016**, *1*, 16141.
- (5) Yonemoto, F.; Nishimura, A.; Motoyama, M.; Tsuchimine, N.; Kobayashi, S.; Iriyama, Y. *J. Power Sources* **2017**, *343*, 207–215.
- (6) Stone, G.; Mullin, S.; Teran, A.; Hallinan, D.; Minor, A.; Hexemer, A.; Balsara, N. *J. Electrochem. Soc.* **2012**, *159*, A222–A227.
- (7) Lin, D.; Liu, Y.; Liang, Z.; Lee, H.-W.; Sun, J.; Wang, H.; Yan, K.; Xie, J.; Cui, Y. *Nat. Nanotechnol.* **2016**, *11*, 626–632.
- (8) Fu, K. K.; Gong, Y.; Liu, B.; Zhu, Y.; Xu, S.; Yao, Y.; Luo, W.; Wang, C.; Lacey, S. D.; Dai, J. *Science Advances* **2017**, *3*, e1601659.
- (9) Luo, W.; Gong, Y. H.; Zhu, Y. Z.; Fu, K. K.; Dai, J. Q.; Lacey, S. D.; Wang, C. W.; Liu, B. Y.; Han, X. G.; Mo, Y. F.; Wachsman, E. D.; Hu, L. B. *J. Am. Chem. Soc.* **2016**, *138*, 12258–12262.
- (10) Han, X.; Gong, Y.; Fu, K.; He, X.; Hitz, G. T.; Dai, J.; Pearse, A.; Liu, B.; Wang, H.; Rubloff, G.; Mo, Y.; Thangadurai, V.; Wachsman, E. D.; Hu, L. *Nat. Mater.* **2016**, *16*, 572–579.
- (11) Takeda, Y.; Yamamoto, O.; Imanishi, N. *Electrochemistry* **2016**, *84*, 210–218.
- (12) Bates, J.; Dudney, N.; Neudecker, B.; Ueda, A.; Evans, C. *Solid State Ionics* **2000**, *135*, 33–45.
- (13) Li, Y.; Li, Y.; Sun, Y.; Butz, B.; Yan, K.; Koh, A. L.; Zhao, J.; Pei, A.; Cui, Y. *Nano Lett.* **2017**, *17*, 5171–5178.
- (14) Steiger, J.; Kramer, D.; Mönig, R. *J. Power Sources* **2014**, *261*, 112–119.
- (15) Tang, C.-Y.; Dillon, S. J. *J. Electrochem. Soc.* **2016**, *163*, A1660–A1665.

- (16) Motoyama, M.; Ejiri, M.; Iriyama, Y. *Electrochemistry* **2014**, *82*, 364–368.
- (17) Motoyama, M.; Ejiri, M.; Iriyama, Y. *J. Electrochem. Soc.* **2015**, *162*, A7067–A7071.
- (18) Santhanagopalan, D.; Qian, D.; McGilvray, T.; Wang, Z.; Wang, F.; Camino, F.; Graetz, J.; Dudney, N.; Meng, Y. S. *J. Phys. Chem. Lett.* **2014**, *5*, 298–303.
- (19) Tsukamoto, R.; Yonemoto, F.; Motoyama, M.; Iriyama, Y. In *In-Situ Cross-Sectional SEM Observations of Li Plating and Stripping on Oxide-Based-Solid-State Electrolytes*, Meeting Abstracts, 2016; The Electrochemical Society; pp 4116–4116.
- (20) Gong, C.; Ruzmetov, D.; Pearse, A.; Ma, D.; Munday, J. N.; Rubloff, G.; Talin, A. A.; Leite, M. S. *ACS Appl. Mater. Interfaces* **2015**, *7*, 26007–26011.
- (21) Leite, M. S.; Ruzmetov, D.; Li, Z.; Bendersky, L. A.; Bartelt, N. C.; Kolmakov, A.; Talin, A. A. *J. Mater. Chem. A* **2014**, *2*, 20552–20559.
- (22) Talin, A. A.; Ruzmetov, D.; Kolmakov, A.; McKelvey, K.; Ware, N.; El Gabaly, F.; Dunn, B.; White, H. S. *ACS Appl. Mater. Interfaces* **2016**, *8*, 32385–32391.
- (23) Massalski, T. B.; Murray, J. *ASM International* **1990**, 1096.
- (24) Michely, T.; Krug, J. *Islands, Mounds, and Atoms*, Vol. 42; Springer Verlag: Berlin Heidelberg, 2004.
- (25) Einax, M.; Dieterich, W.; Maass, P. *Rev. Mod. Phys.* **2013**, *85*, 921.
- (26) Seiler, H. *J. Appl. Phys.* **1983**, *54*, R1–R18.
- (27) Lin, Y.; Joy, D. C. *Surf. Interface Anal.* **2005**, *37*, 895–900.
- (28) Cahn, R. W.; Haasen, P. *Physical Metallurgy*; North-Holland: Amsterdam, 1983.
- (29) Pei, A.; Zheng, G.; Shi, F.; Li, Y.; Cui, Y. *Nano Lett.* **2017**, *17*, 1132–1139.
- (30) Balke, N.; Jesse, S.; Kim, Y.; Adamczyk, L.; Tselev, A.; Ivanov, I. N.; Dudney, N. J.; Kalinin, S. V. *Nano Lett.* **2010**, *10*, 3420–3425.
- (31) Hoenigman, J.; Keil, R. *Appl. Surf. Sci.* **1984**, *18*, 207–222.
- (32) Deal, B. E.; Grove, A. *J. Appl. Phys.* **1965**, *36*, 3770–3778.
- (33) Dologlou, E. *Glass Phys. Chem.* **2010**, *36*, 570–574.
- (34) Oishi, Y.; Kamei, Y.; Akiyama, M.; Yanagi, T. *J. Nucl. Mater.* **1979**, *87*, 341–344.
- (35) Zhang, R. Q.; Lifshitz, Y.; Lee, S. T. *Adv. Mater.* **2003**, *15*, 635–640.
- (36) Zheng, H.; Liu, Y.; Mao, S. X.; Wang, J.; Huang, J. Y. *Sci. Rep.* **2012**, *2*, 542.
- (37) Oniciu, L.; Mureşan, L. *J. Appl. Electrochem.* **1991**, *21*, 565–574.
- (38) Ostadhosseini, A.; Kim, S.-Y.; Cubuk, E. D.; Qi, Y.; van Duin, A. C. *J. Phys. Chem. A* **2016**, *120*, 2114–2127.
- (39) Sen, F. G.; Alpas, A. T.; Van Duin, A. C.; Qi, Y. *Nat. Commun.* **2014**, *5*, 3959.
- (40) Coburn, J.; Winters, H. F. *J. Appl. Phys.* **1979**, *50*, 3189–3196.